Experimental Study of Shock/Shock Interferences in a Hypersonic Mach 20.2 Rarefied Flow

Vincente Cardona[1], Viviana Lago[2]

Abstract

When a spacecraft re-enters Earth's atmosphere, or in the case of a destructive space debris re-entry, the problem of proximal bodies is considered. In particular shock/shock interferences can occur, and affect the structure of the spacecraft or the debris aerodynamics. Depending on the altitude, endured flows are hypersonic and rarefied, leading to predominant viscous effects. In order to better understand the impact of rarefaction level on shock/shock interferences, experiments were carried out in the MARHy wind tunnel (ICARE, CNRS, France). A couple of spheres were placed in a hypersonic rarefied flow with a free-stream Mach number of 20.2 and a free-stream pressure of 0.07 Pa. Different relative positions were experimentally explored to identify various types of interferences occurring in this flow, characteristic of an altitude of 95 km. Results, obtained with the discharge glow visualization method, allowed the detection of shock waves and the analysis of intensity levels. They revealed that shock-shock interferences show different behaviors than in a continuum regime or in a less rarefied flow. Indeed shock waves do not seem to be affected by the interaction with an incident shock. However, by analyzing the level of intensity near the interacting sphere, differences are observed according the different positions. This statement is also true concerning the drag forces, measured on the second sphere with the pendulum technique. This study shows that even if the shock/shock interferences are not clearly observed visually, the aerodynamics of the following sphere is modified according its position towards the first one. As a consequence, it can be stated that during the atmospheric re-entry, the shock/shock interferences play a part on wall flux endured by the spacecraft structure and on the modification of space debris trajectory.

Keywords: *Hypersonic, Rarefied Flow, Shock/Shock interferences, Wind tunnel*

1. Introduction

When re-entering the atmosphere, spacecraft, or space debris suffers hypersonic flows. For a spacecraft flying back to Earth, it is wished to preserve its structure, so that it does not burst in the atmosphere. To do so, it is important to design the geometry of spacecraft so that no shock/shock interactions can add damages to the already high temperatures of a re-entry. In the case of the re-entry of space debris, it is known that most of them fragment due to high thermal and pressure load. These multiple fragments can interact on each other, modifying their trajectory.

Due to the nature of the Earth's atmosphere, different flow regimes are experienced by the re-entering objects. First, at very high altitude, the regime is free-molecular and no compression of fluid is observed. Then, with the decrease in altitude the objects pass through slip and transitional regimes between around 120 and 40 km in altitude. There, the density progressively increases thanks to the terrestrial gravitational effect. These rarefied regimes are characterized by viscous effects and by the development of thick and diffuse shock-waves. Finally, the flying object reaches the continuum regime which is characteristic of our known living environment.

The work presented here aims to study the fluid dynamics of proximal bodies in the early stage of

[1]*CNRS, ICARE, UPR 3021, 1c av. de la Recherche Scientifique, CS 50060, F-45071, Orléans cedex 2, France, vincente.cardona@cnrs-orleans.fr*

[2]*CNRS, ICARE, UPR 3021, 1c av. de la Recherche Scientifique, CS 50060, F-45071, Orléans cedex 2, France, viviana.lago@cnrs-orleans.fr*

atmospheric re-entry, and more specifically the shock/shock interferences first described by Edney [1]. For this purpose an experimental study is proposed in a hypersonic rarefied flow. Such flow conditions are still poorly understand and this work aim to bring some results to improve our knowledge and thus calculations. Indeed, the problem proposed here take into account multiple complex physics: hypersonic flows, rarefied effects, and aerodynamic interactions.

In a continuum regime, hypersonic flows are characterized by strong shock-waves, thus a shock/shock or shock/boundary layer interaction leads to important viscous interaction [2]. The concerned surface sees an increase in pressure and temperatures at its wall [3]. If the topic has been studied a lot in a continuum regime [4, 5, 6, 7, 8, 9, 10], the rarefaction effects of the slip and transitional regimes are rarely studied. Indeed, some numerical results are found[11, 12], but experimentally, only slightly rarefied flows [3, 13, 14], or supersonic rarefied flows [15] are found.

By means of two diagnosis, we propose to investigate the shock/shock interferences occurring between two spherical model in a hypersonic rarefied flows. A first sphere is fixed in the flowfield, while a second sphere will be moved behind it to observe its different behaviors according its position. A first experiment will allow to visualize the flow-field around the spheres, while a second experiment, based on a pendulum technique, will give the drag forces endured by the following spheres.

2. Experimental conditions
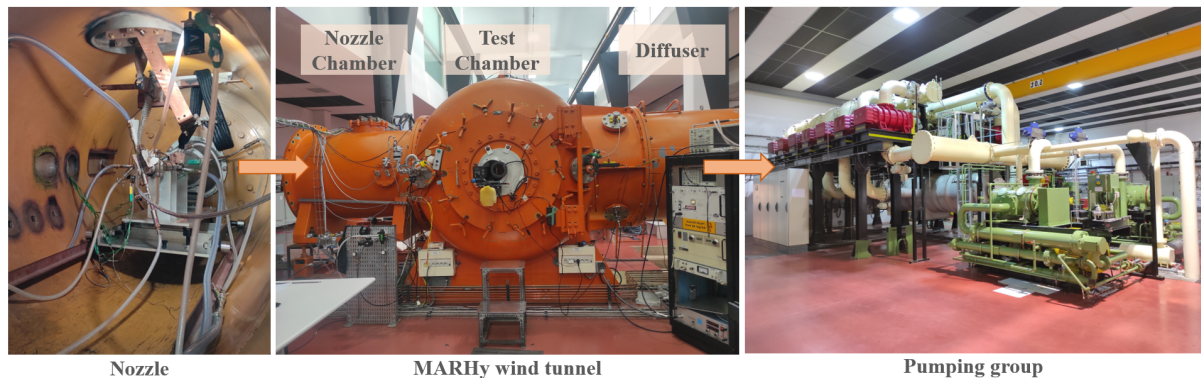### 2.1. MARHy wind tunnel

Fig 1. The MARHy wind tunnel

The experiments were carried out in the MARHy wind tunnel presented in Fig.1. The facility, based at ICARE, CNRS (Orléans, France) can reach Mach numbers from 0.8 to 20.2 with different levels of rarefaction thanks to a large set of interchangeable nozzles. It allows to generate cold flows which experimentally simulate flights in Earth's atmosphere, at altitude ranging between 50 and 110 km.

The wind tunnel is composed with three major parts: the nozzle chamber in wich is placed the nozzle and where the gas come from (left picture of Fig.1), the test chamber where are obtained the free-stream flow conditions, and the diffuser that links the test chamber to the pumping group (rigth image of Fig.1) which ensures good vacuuming conditions with no limit in time.

2.2. Flow conditions

For this study, the chosen nozzle delivers a Mach 20.2 flow with a free-stream pressure of 0.07 Pa. The detailed working conditions are presented in Table 1, where the stagnation conditions refer to the conditions at the nozzle throat (subscript $_0$) and the free-stream conditions those in the test chamber (subscript $_\infty$).

The flow is obtained as explained in the following. First of all, the wind tunnel is hermetically closed and vacuumed thanks to the powerful pumping group. In hypersonic conditions, as presented in this work, all the pumps shown in Fig.1 need to work to ensure a constant vacuuming. Thus, two primary pumps and thirteen Roots type pumps allow an airflow of 48850 $m^3.h^{-1}$ so that the free-stream conditions exposed in Table.1 are constantly obtained.

Table 1. Flow conditions in the MARHy wind tunnel for the M 20.2 - 0.07 Pa nozzle.

Stagnation conditions			Free-stream conditions		
gas		N_2	gas		N_2
p_0	(Pa)	$3.5.10^5$	p_∞	(Pa)	0.07
T_0	(K)	1100	T_∞	(K)	13
ρ_0	(kg.m^{-3})	1.07	ρ_∞	(kg.m^{-3})	$1.73.10^{-5}$
			μ_∞	(Pa.s)	$9.15.10^{-7}$
			Re_{u_∞}	(m^{-1})	$2.84.10^4$
			Ma_∞		20.2
			λ_∞	m	$0.77.10^{-3}$

The MARHy wind tunnel works with dinitrogren. The gas comes from a 200 bar rack of 8 cylinders and goes in the nozzle, being regulated by a two stage adjustable pressure reducer. To obtain the good flow conditions, the gas needs to be heated so that the gas is fully expanded and does not freeze. The gas is heated by conduction, passing through a graphite resistance powered by a 20 kW electrical source and so heated by Joule effect. The temperature at the nozzle throat is regulated by choosing the right number of delivered amperage (around 800 A). The entire nozzle (electric source, heater, nozzle throat, and the divergent) is cooled by a water system to ensure the good operating conditions of the nozzle and the flow.

The pressure at the throat of the nozzle is monitored by Omega PXM419 pressure sensor, accurate at 0.08%. All the temperatures are monitored by type K thermocouples, accurate at 1 K.

The obtained free-stream is laminar and can last for several hours without discontinuities. The core is not isotropic but the whatever the position of the models, conditions are known. Thus, results can be corrected with real experimental conditions.

2.3. Models and simulated conditions

As for many studies on proximal bodies, considered models are blunt shaped. The chosen models are a couple of 18 mm-diameter spheres in boron nitride. This material is resistant at high temperature and do not conduct electricity. Thus, the models cannot break or deform with slightly high temperatures (maximum 500 K), and the visualization method (ionization) will not modify the electric field around models. Both spheres are covered with a thin layer of black spray paint to intensify the contrast of the visualization method. The size of the models is chosen for two reasons: not too big so that they both feet in the diameter of the core (12 cm), and not too little to be instrumented for multiple types of studies.

Regarding the free-stream flow and the size of one sphere, the Knudsen number is of $4.28.10^{-2}$, which is representative of the slip regime. To estimate the experimental simulated altitudes, the Tsien number ($\sigma = Ma_\infty / \sqrt{Re_\infty}$) is chosen. Indeed, it takes into account both the velocity and the viscous effects, enabling to characterize the dynamic rarefaction level of the flow. Considering Prévereaud *et.al* [16] work, the velocity of a 1 m-diameter sphere re-entering the atmosphere is known for altitudes ranging between 0 and 78 km. By extrapolating their results and calculating the associated Mach and Reynolds numbers with the atmospheric parameters of the NRLMIS Atmosphere Model [17], the Tsien number has been calculated for altitudes up to 120 km. By analogy, with the flow conditions exposed in Table 1, the 18 mm-diameter model is representative of a 1 m-diameter sphere flying at 95 km in altitude.

3. Experimental devices and post-processing

In order to study the shock/shock interferences, the two models were placed in the free-stream flow, representative of a piece of debris, followed by one fragment. The purpose is to analyze and understand the aerodynamic properties of the interaction between two spheres according the relative position of the following spheres towards the other one. Two types of experiments were realized to investigate this topic. First, a visualization of the flow field around models were obtained thanks to the glow discharge

technique. The second study consists in measuring the drag forces of the following sphere using a pendulum technique.

3.1. General set-up
The general set-up is schematically exposed in Fig.2 to clarify our work.
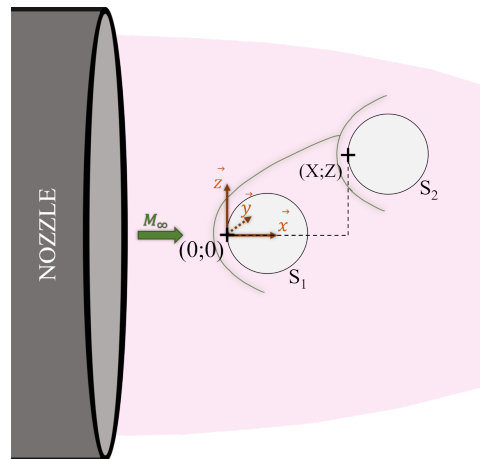

Fig 2. Schematics of the general set-up.

For both the visualization and drag measurement experiments, the first sphere (S_1) is held the same way. S_1 is aligned with the center of the nozzle in the $\vec{y}$ and $\vec{z}$ directions. It is placed 45 mm from the exit of the nozzle in the $\vec{x}$ direction. S_1 is held in position by a vertical profiled support mounted on a rotary system, so that is can be removed from the flow. Since S_1 is in a fixed position, its stagnation point is taken as the origin of the spatial referential.

For both the visualization and drag measurement experiments, the following sphere, S_2, is also aligned with the center of the nozzle in the $\vec{y}$ direction.
However, depending on the experiments, the support of S_2 varies. For the visualization, S_2 is held by a horizontal profiled support coming from the rear. For the drag forces measurement, it is suspended by a pendulum system, which will be more detailed in a specific section. In both experiments, the maintaining system of S_2 is mounted on a tri-axial displacement robot. This allows to modify the coordinates (X,Z) of S_2, and also to remove it from the flow.

3.2. Flow-field visualization
3.2.1. Glow discharge technique
The shock/shock interferences were first studied with the visualization technique at our specific flow conditions. In the rarefied flow presented here, the density is too low to observe any index variation of gas that would be due to molecules compression. Thus, methods such as Schlieren or PIV, for example, can not be applied.
The technique used is called the glow-discharge. It consists in weakly ionizing the flow by applying a negative voltage of -2kV on a copper cathode placed around the flow, at the exit of the nozzle. This method illuminates particles such as the level of intensity is representative of the density of molecules. There is no direct proportional ratio between the luminosity and the local density. Indeed, the illumination generated by the ionization is volumetric, and recorded images are the result of a luminous integration on the line of sight of the camera. However, this allows to analyze the variations of density near shock/shock interferences.

3.2.2. Image acquisition and post-processing
The images are recorded with a Kuro CMOS camera with back-illuminated technology. The camera is equipped with a VUV objective lens which gives a resolution of 0.153 μm.px^{-1}. For each relative positions explored, three sets of 20 images are recorded. The global density of the flow-field being

low, the luminous intensity is low, this is why a long exposure time of 200 ms is needed to obtain clear images. This is made possible since the flow is steady and laminar. The three sets of images are the following:

- The two spheres are in the flow.

- The first sphere is removed from the flow, so only the second sphere is in the flow. Indeed, due to the anisotropic nature of the flow, S_2 in interaction will be compared to S_2 without interaction, at the same position (X,Z) towards the exit of the nozzle.

- Both spheres are out of the flow, so that only the background is recorded.

The post-processing of images is explained with the example given in Fig.3 for two interacting spheres. Each set of images is averaged so that the noise is limited. The mean image with one or two spheres (a) and the mean image of the background (b) present a luminous gradient in the $\vec{x}$ direction due to the location of the ionizing source. By dividing image (a) with image (b), a normalized image is obtained (c), where there is no more luminous gradient and where shock waves can be observed. By applying the Fourier Self-Deconvolution (FSD) detailed by Kovacs $et.al$ [18], thick and diffuse shock waves of rarefied flows can be detected. As shown in (d), three regions are observed: the boundary layer (BL), the middle of shock (MS), and the foot of shock (FS). The method is based on the analysis of luminous intensity on each horizontal line of pixels, in the direction of the flow (from left to right). It allows to detect the location of the point of maximum luminous intensity, which corresponds to the boundary layer near the model. The FSD filters the luminous signal, and allows to find the beginning of the luminosity increase (upstream the sphere). This point corresponds to the foot of shock. In between these points, the inflection point of the luminous intensity gives the location of the middle of shock.
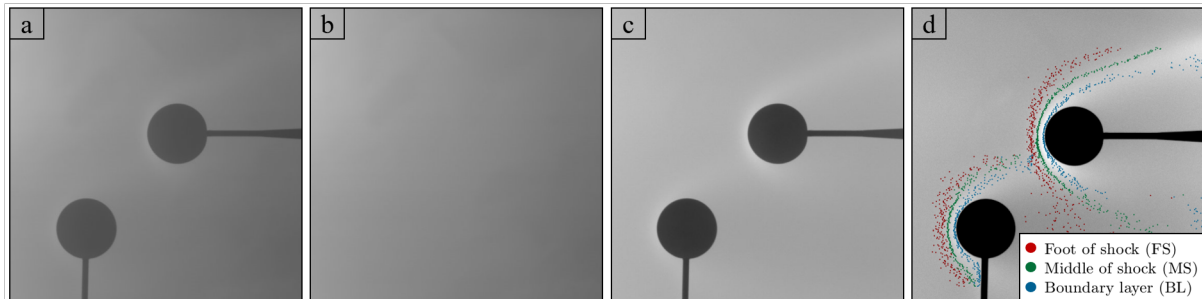

Fig 3. Post-processing of images: a) mean image of the flow around spheres; b) mean image of the flow without spheres; c) normalized image of the flow around spheres; d) shock-wave detection method.

On normalized images, the analysis of shock waves and intensity levels gives some points of interest that are described through the schematics of Fig.4. In schemes a) are presented the stand-off distances Δ for a sphere. These distances will be noted for S_2 in interaction, and for S_2 alone in the free-stream. They correspond to the distance between the stagnation point of each sphere to its three shock-wave regions. In b) are shown the points of interest in the interference area (around S_2 in interaction). P_i is the intersection point between the incident middle of shock and the second sphere middle of shock. It is described by its distance d_i toward the surface of S_2, and by the angle Θ_i between the segment $[P_i\ C_2]$, where C_2 is the center of S_2, and the horizontal. The shock wave being diffused, d_i and Θ_i are determined by averaging the two opposite points in the intersection area. Finally, P_{ml} represents the point of maximum intensity in the interference area. It is also defined with its distance d_{ml} toward the surface of S_2, and with its angle Θ_{ml} between the segment $[P_{ml}\ C_2]$ and the horizontal.
It is to be noted that an analysis of the intensity level will be made at P_{ml} and also at the brighter point on the stagnation line of the spheres, corresponding to the level of intensity in the boundary layer.
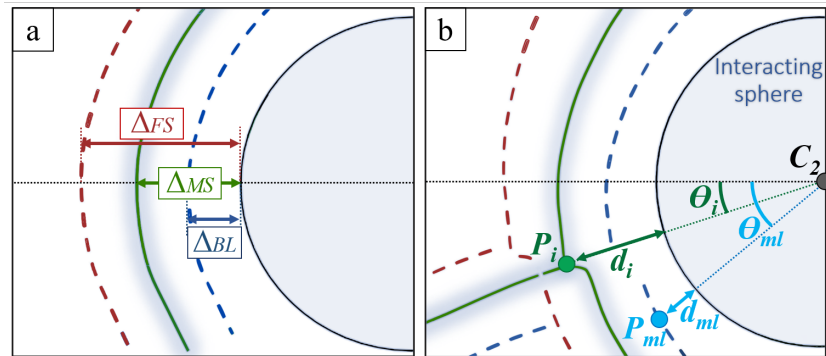
Fig 4. Points of interest on images: a) stand-off distances of the foot of shock (Δ_{FS}), middle of shock (Δ_{MS}) and boundary layer (Δ_{BL}) of a sphere ; b) points of middle shocks intersection P_i and of maximum luminosity in the interference area $P_m l$ around S_2.

3.3. Drag force measurement

3.3.1. Pendulum technique

In this paper, the measurement of drag forces endured by the second sphere is realized thanks to the pendulum technique. As seen in Fig.5, it consists in suspending a sphere in a flow. The suspended sphere, which mass is of 6.93 g, is drilled in its center. A thin non-elastic wire, made of enameled Teflon, passes through the sphere and is attached to an horizontal tube itself fixed to a tri-axial displacement robot. The wire is of 0.1 mm in diameter which is lower than the mean free path of the flow field (0.77 mm). This way, the flow does not exercises any forces on the wire. To ensure the transversal centering of the sphere (in the $\vec{y}$ direction), both sides of the wire are equal in length, and S_2 is glued to the wire so that it cannot slide along the wire. Thus, the sphere only responds to the flow in the $\vec{x}$ direction.

Fig 5. Image of the pendulum set-up.

The pendulum technique can be applied in two different ways. For the first method (fixed position), the sphere is positioned where desired and a series of 100 images is taken. For the second method (measurement in motion), the sphere is placed at an initial position and then its support is moved in the $\vec{z}$ direction or in the $\vec{x}$ direction. To follow the trajectory of S_2, as many images as necessary are recorded (around 3000 for each trajectory). Whatever the method used, each image of a series is recorded with an exposure time of 20 ms so that the objects are not blurred.

3.3.2. Force calculation

As described by Cardona and Lago [19], the force calculation is based on the measure of the wire's angle towards the vertical. According the position of S_2 in the camera field, a correction of angle is necessary to take into account the camera bias. The drag force is calculated with the Eq.1, where m is the mass of S_2 (in kg), g is the gravitational acceleration (g=9.81 m.s^{-2}), and α is the angle of the wire towards the vertical (in degree).

$$F_x = m.g.sin(\alpha) \tag{1}$$

The wire is detected manually, and a ± 1 px of accuracy on the detection of the center of the sphere is estimated. For the fixed position method, the drag force is averaged of the series of 100 images, and its error is given by calculating the standard deviation. For the moving trajectory since no averaging can be realized, a maximal accuracy is calculated based on the maximal clicking error possible. The angle is estimate accurate with $\pm 0.9^o$ and consequently the force with ± 1.1 mN.

The previous work [19] allowed to validate this method of measurement. Indeed, results were compared to another drag measurement device [20], and to the literature [21, 22, 23], and a good accordance was found.

As for images, the measurement of the drag force of a single sphere were measured at different positions in the flow-field. This way, it is possible to estimate correctly the impact of shock/shock interferences on the aerodynamics of the flow, independently of the slight variation of pressure and Mach number of the anisotropic core.

4. Results and discussion

4.1. Image analysis

Images were recorded for a vertical displacement of S_2. Its longitudinal X coordinate is fixed at 27 mm from the stagnation point of S_1 while its Z coordinate varies. This way it is possible to explore different types of shock/shock interferences. Two aspects of the shock wave of S_2 will be explored: the shock wave deformation and the variation in intensity level, representative of the local density of the flow.

4.1.1. Shock deformation due to interactions

With the normalized images, as observed in image c) of Fig.3, shock wave are hardly perceptible. This is why, to improve the contrast of the flow-field, a change of colormap (from gray to jet) is realized. The contrasts is improved by cutting the lowest values of intensities, while being careful to only cut the values that concerns the models. Note that the contrasting is only realized for visual reasons. The shock-wave detection or the analysis of the intensity values were realized on normalized images, without modifying contrasts. The results of the visualization improvement are observed in Fig.6, where six relative positions allow to evaluate the evolution of the flow-field around S_2.

As shown in this selection of images, whatever the relative position observed, the intensity seems higher around S_2 than at the stagnation point of S_1. This would mean that the shock/shock interferences have a direct impact on the local density at the wall of the following object. However, the flow being non-isotropic, a deeper qualitative study will be made later in this work, that tends to confirm those thoughts. The denser region is described by the red area. By increasing the angle of interaction Θ_i (decreasing the altitude of S_2), the denser region displaces from the bottom of the sphere to its top, where it is mostly located. Indeed, whatever the position, the red area is observed above the sphere, which is not the case below it. Moreover, it seems that the highest values (dark red) are only observed in front of the sphere or on its top. This lets think that the efforts exercised on S_2 also follow this tendency, pushing it down in the wake of S_1 in most positions. A measurement of the lift forces will be necessary to confirm this statement.

Another remark can be made concerning the thickening of S_2 shock wave behind the sphere. It seems that the more S_2 enters the wake of S_1, the more the rear part of its shock diffuses and gets red. Regarding the cases $\Theta_i > 18°$ (the three bottom images of Fig.6), the two shock waves seem to merge. Thus, it is possible that they create a more compressed area than in the shock-wave of a single sphere. Moreover, since S_2 is mostly located in the wake of S_1, the rarefaction level is higher than in the free-
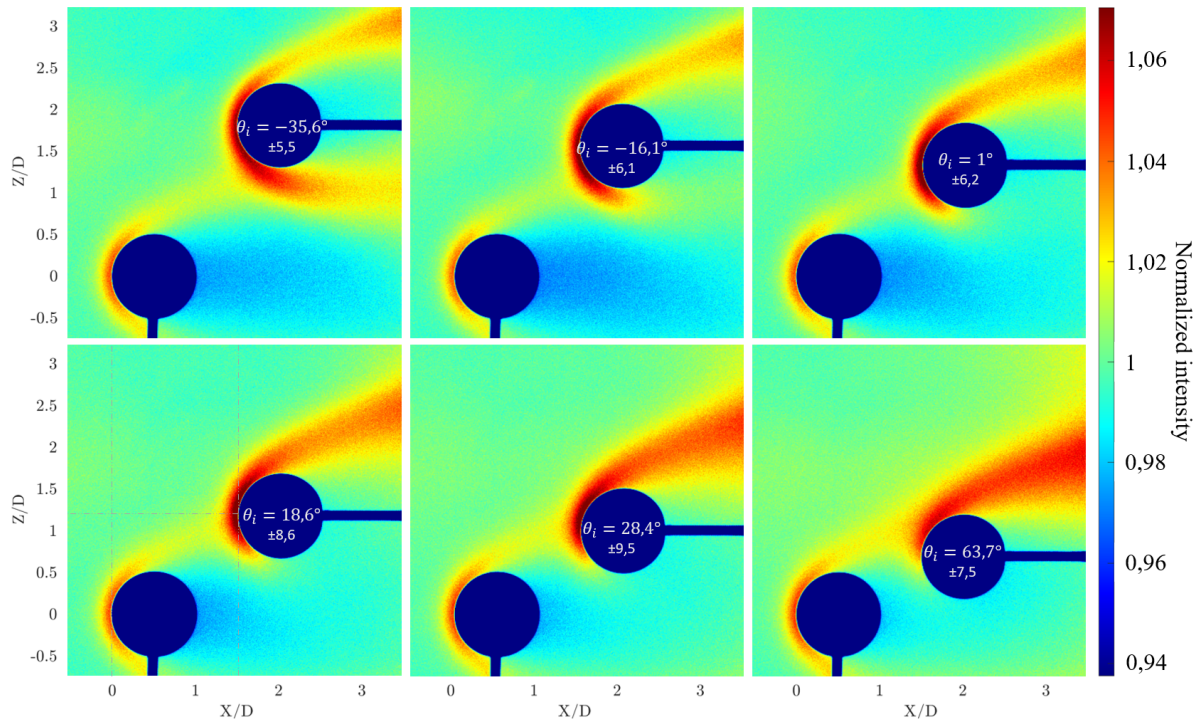
Fig 6. Selection of experimental normalized images with a jet colormap.

stream. Which means that behind S_2 there is even less molecules, so the shock diffuses and spread in the direction of the empty space.

Moreover, if looking at the shock-wave shape, no real deformation are shown in the interference area. In Fig.7, are presented the middles of shock S_2 in interaction with S_1 (yellow). These shock waves are compared with the shock waves of the reference cases. As explained before, due to the anisotropy of the flow, each position needs its own reference. This means that for every position, S_2 is also observed alone in the free-stream, at the exact same location than in interaction (purple).

Here, it can be observed that only the lower part of S_2 shock wave is modified, certainly due to a very low molecular density in the wake of S_1, preventing them from forming a strong shock-wave. But in the interaction area, no pattern seems to appear, contrarily to continuum [1, 24] or less rarefied flows [25, 15, 11].

Fig.8 presents the stand-off distances of the three regions of the shock waves for S_2 in interaction, and for $S_{2_{ref}}$ (S_2 alone in the free-stream).

As can be observed, no tendency seems to appear that would have highlighted a certain behavior according the position of S_2 when interacting with S_1. It is to be noted that, even for the low position (high Θ_i), where the rarefaction increases since S_2 penetrates the wake of S_1, no increase of the shock wave stand-off is shown, contrarily to what expected and observed in previous supersonic rarefied studies [26].

In order to deepen the comparison of shock-waves, a particular interest has been taken on the point of intersection of the middle shocks P_i, and on the point of maximal luminosity P_{ml}. Their distance to the surface of S_2 are plotted according the angle of interaction in Fig.9. By definition (see Fig.4), P_i is associated to the middle shock and P_{ml} to the boundary layer of S_2. To see a deformation of the shock waves due to the interaction, d_i and d_{ml} have to be compared respectively with $d_{MS_{2_{ref}}}$ (the distance of the non-deformed middle shock towards the surface of $S_{2_{ref}}$), and with $d_{BL_{2_{ref}}}$ (the distance of the
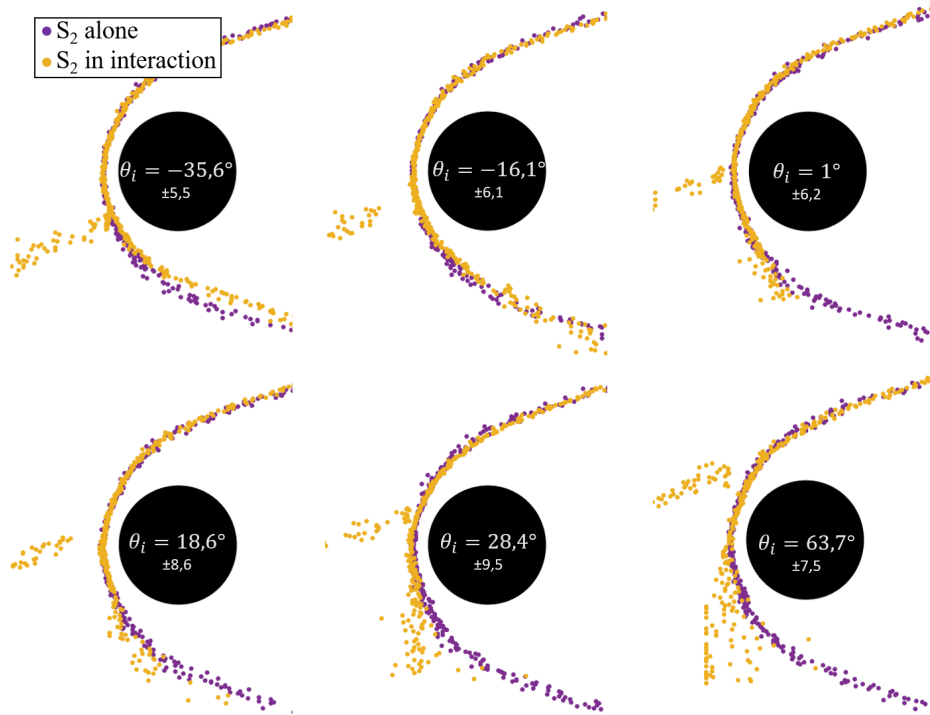
Fig 7. Superposition of S_2 middle shock without (purple points) and with (yellow points) interaction.

non-deformed boundary layer towards the surface of $S_{2_{ref}}$).

Since the shock wave of S_2 depends on its location, the shapes of its three regions vary too. Thus, on the two graphs of Fig.9, $d_{MS_{2_{ref}}}$ and $d_{BL_{2_{ref}}}$ are plotted for two altitudes: the highest (purple) and lowest (pink) positions shown in Fig.6. For each one, a vertical line is drawn to represent the angle associated to its altitude. This way, if looking at the negative angles, the reference should be taken as the purple curve, while for positive angle, the pink reference is more appropriate.

In the left graph of Fig.9, even if the green points are in the standard deviation of references, a slight tendency of d_i towards the reference can be observed. Looking at the negative angles (when S_2 is high behind S_1), it seems that the point of interaction P_i distances itself from the reference middle shock, represented by the purple curve. On the contrary, for positive angles (when S_2 is low behind S_1), P_i seems to get closer from the pink reference.

For the most luminous point distance observed in the right graph, the two reference values are equivalent so no distinction will be made. Around -20°, d_{ml} seems to increase according to the reference, while the rest of the points show a linear behavior. At the extreme angle (63.7°) P_{ml} is way closer to the surface of S_2. Either this is due to the fact that the shock really deforms itself, or it could be a singularity of measurement. To make a clear statement, more points would be needed in between 30 and 60°.

This two graph show that there is a setback area on the negative angle which means that a slight deformation of shock waves is observed for the higher positions. The study of shock/shock interferences in a Mach 4 - 2.67 Pa and 8 Pa [26] already showed a setback area at the interaction point for SSI type I to IV, in the negative angles. In the present work, the setback area is not as clear as for the previous studies, but still is slightly noticeable thanks to the distances of P_i and P_{ml}.

4.1.2. Evolution of the level of luminous intensity

The normalized images, in addition to the shock-wave observation, allows to obtain a first look at the local density. Even if the level of intensity is not directly proportional to the local density, it still gives an overview of the differences observed for positions of S_2 behind S_1. In Fig.10, the left graph represents the normalized intensities of the brighter pixel at the stagnation point of the spheres and of the point of
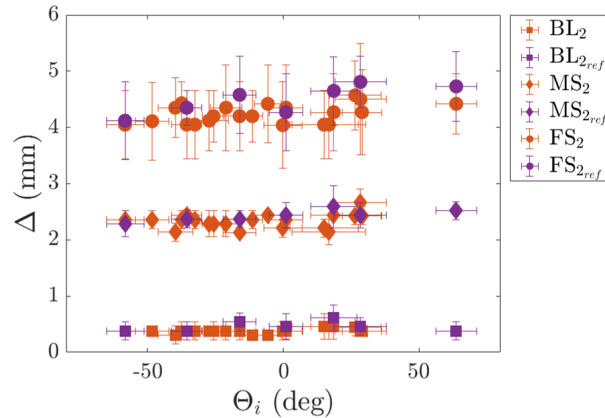
Fig 8. Standoff distances according the position of S_2 in the flow, defined by Θ_i, the interaction angle.

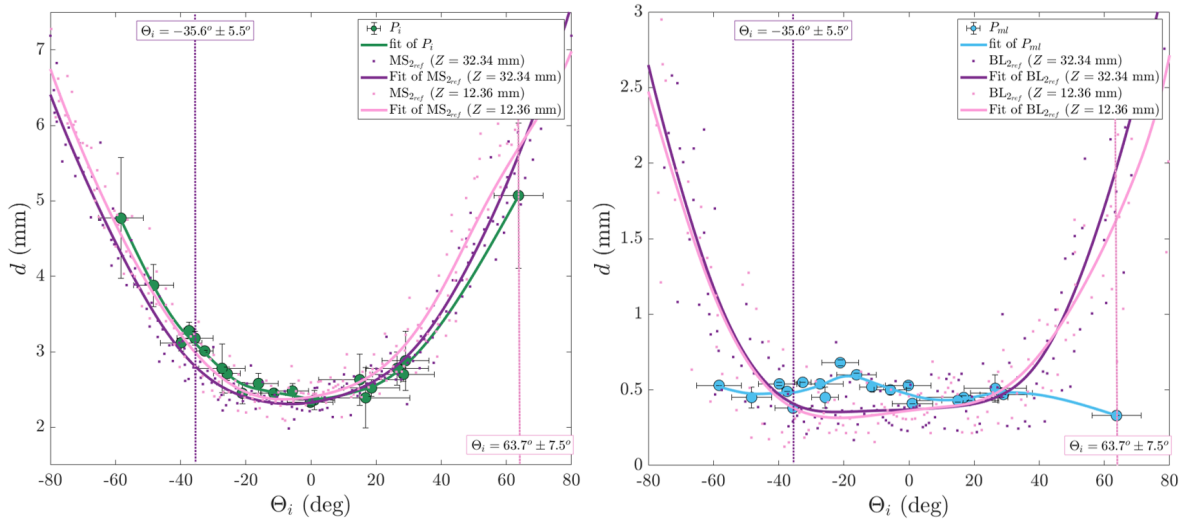**Fig 9.** Left graph : distance of the interaction point P_i compared to the middle shock distance of S_2 without interaction for two altitudes. Right : distance of the most luminous point P_{ml} compared to the boundary layer distance of S_2 without interaction for two altitudes.

maximal intensity in the interaction area (P_{ml}). As can be observed, contrarily to the intensity of S_1, the intensity of $S_{2_{ref}}$ changes according its position in the flow. This is due to the variation of free-stream Mach number and pressure generated by the non-isotropic core. To evaluate only the impact of the shock/shock interactions, this intensities are corrected so that the reference is constant and equal to the value of S_1 which is located in the perfect conditions. Results of this calculation are shown on the right graph of Fig.10.

Either at the stagnation point (I_2) or at P_{ml} (I_{ml}), a clear evolution of the intensity is shown: from -60° to around 10°, the intensity increases, and then it decreases while S_2 penetrates the wake of S_1. With this information, the maximal wall pressure peak is expected to occur for the position where the angle of interaction is around 10°.

At the stagnation point, above 40°, the value even cross the reference, which means that the local density is lower than in free-stream. This phenomenon was expected since, as S_2 enters deeper in the wake of S_1, the rarefaction level increases. Since no evolution was observed in terms of stand-off distances, the impact of rarefaction level, at such velocities, was reconsidered. The luminosity showing an evolution, it allows to confirm the existence of the rarefaction level impact.
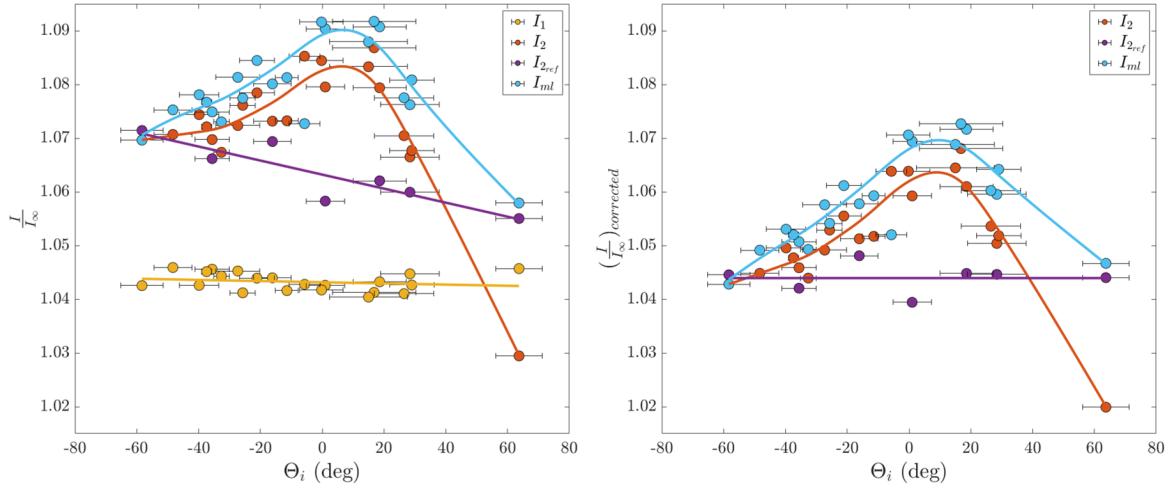
Fig 10. Left graph : Normalized maximal intensity at the stagnation point of S_1, S_2 in interaction and S_2 without interaction, and Normalized intensity at P_{ml}. Right graph : Normalized intensities corrected according the reference value (S_2 without interaction).

In consequence, it is difficult to identify different type of interactions, even-though different distributions of the flow seems to appear. It seems that the shock/shock interferences, as described by Edney [1] do no exist here. Usually, shock/shock interference generates strong impact on a small area, each defined by a specificity. These types of interferences were observed in a Mach 4 - 2.67 Pa or 8 Pa [26] flows. But here, the interfering shock waves seems to merge, creating a large shock/shock mixing layer : no real deformation of the shock waves are observed, and an increase of the density level is present. An electron gun is being developed, and hopefully will help deepen this phenomena and give a more accurate vision of the physics. For now, it can be stated that even if the flow has hypersonic velocities, the viscous effect are predominant, and attenuate the impact of an incident shock interacting with a bow shock.

In the next section, a quantitative study based on the measurement of drag forces will complete the image analysis. Drag forces allow to evaluate the evolution of the aerodynamics of S_2 according its position behind S_1.

4.2. Drag force measurement
As explained, drag forces were recorded in two different manners: in a fixed position, or in movement.

4.2.1. Measurement at fixed positions
For the fixed position method, the suspended sphere is placed wherever it is desired in the flow, accepting a slight pendulum movement. The measurement consists in recording a set of 100 images, and for each image, the drag force is calculated. As seen in left graph of Fig.11, the pendulum movement generate a sinusoidal measured force. These values are averaged and the standard deviation is calculated, which gives for each position a mean drag value with a certain accuracy.
These values are reported according the altitude of the spheres in the right graph of Fig.11. As the free-stream flow is non-isotropic, the drag force of a single sphere ($S_{2_{ref}}$) was measured at the center of the core, and at a higher altitude. Since the evolution of the free-stream pressure is linear according Z, only two measurements were realized. The real value of the drag force of a single sphere of 18 mm-diameter is for $Z = 0 : F_x = 8.69 \pm 0.63$ mN. The orange points are the measured drag forces exercised on S_2 when in interaction with S_1. These measurements were realized for the positions exposed in Fig.7, where $X = 27$ mm.
It has been chosen to correct the measured values according the altitude Z in order to observe only

the variation due to the shock/shock interactions. Fig.12 shows the corrected drag forces according the angle of interaction between the middle of shocks.
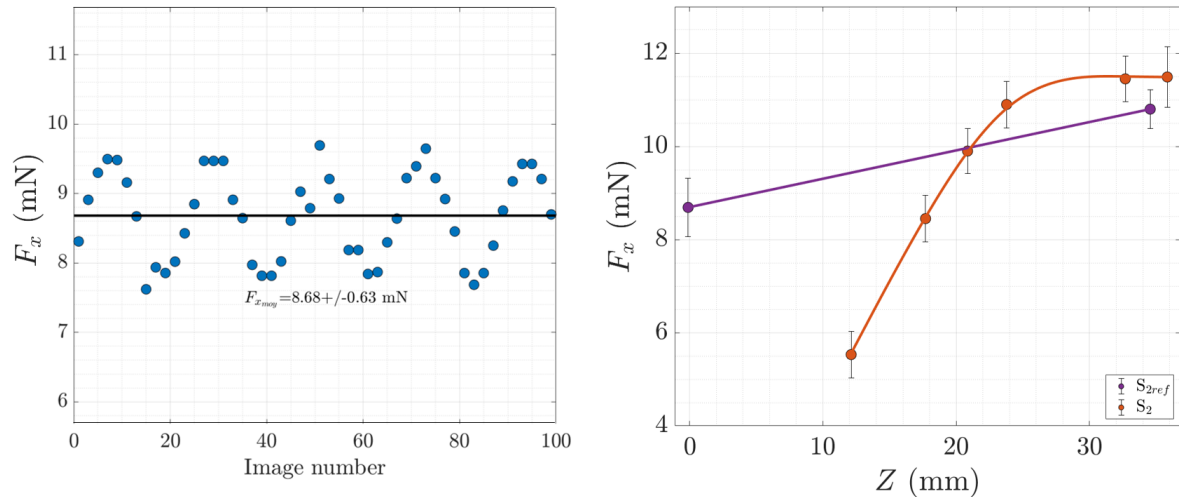

Fig 11. Drag forces of a suspended sphere, fixed in position. Left: forces of a single sphere for each image of the records. Right: mean forces of a single sphere at two altitudes (purple), and of the interacting sphere (orange) according the different altitudes presented in Fig.6.
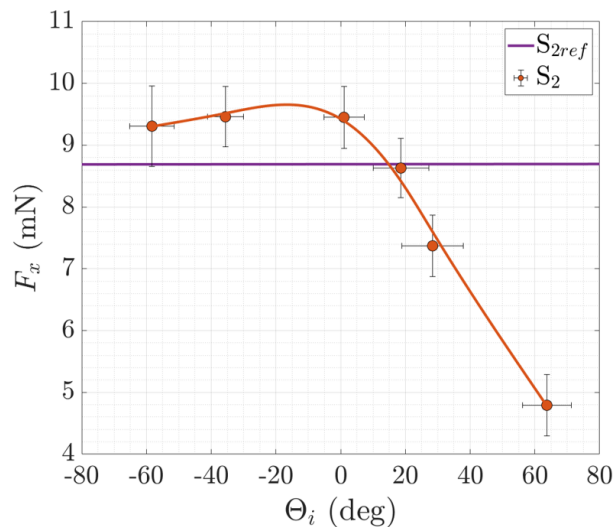

Fig 12. Corrected drag forces according the angle of interaction.

As observed, the drag force shows a real variation according the location of S_2 towards S_1. When S_2 is mostly above the shock wave of S_1 ($\Theta_i \approx$ -60°), its drag force is higher than the reference one, which means that S_2 is not high enough from S_1 not to be influenced by its flow-field. While entering the wake of S_1, the drag force keeps increasing until around -10°, where it reaches a maximum. As a reminder, a deformation of the boundary layer were observed around -20° in the right graph of Fig.9. This might an indication of the most powerful shock/shock interferences in these conditions. Then, the drag force drastically decreases, and from around 15° reaches values that are lower than the reference case. At this point, it can be said that S_2 is mostly located in the wake of S_1, where the rarefaction level is high enough to protect S_2 from being pushed away by the flow.

The study with fixed positions allowed to determine with a better accuracy the force at the desired positions. But due to the low pressure, it requires a lot of time for the sphere to stabilize before recording the images. This is why another technique is adopted to enlarge the number of results.

4.2.2. Measurement in motion

This technique consists in measuring forces while the suspended sphere (S_2) is in motion. The initial position of S_2 is chosen, and then the support is moved up in the $\vec{z}$ direction, letting S_2 swing in the flow. This way, the sphere displaces itself in the flow according the forces it endures, describing a trajectory as shown in Fig.13. It can be observed, regarding the dispersion of the points, that S_2 still has a sinusoidal movement.
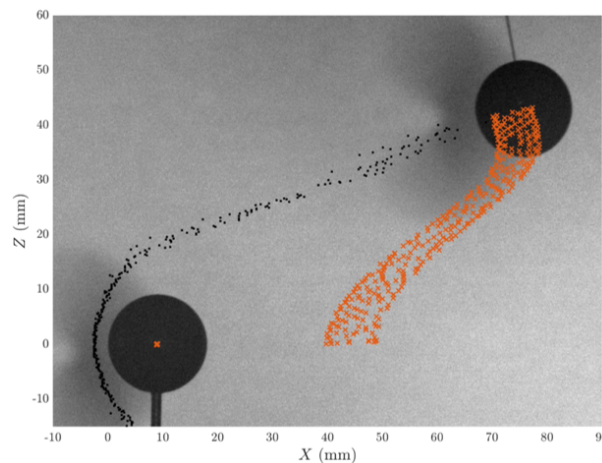

Fig 13. Example of trajectory described by the suspended sphere in motion.

With the large number of images (around 3000 for each trajectory), the path can be averaged along with the values of drag forces. Due to the gradient of pressure in the free-stream flow in the $\vec{z}$ direction, the forces need to be corrected as for the measurements with fixed positions. Results of this work are shown in Fig.14. On the left graph are represented the averaged trajectories colored according the corrected drag forces. On the right, an interpolation has been realized to better visualize the distribution of drag forces perceived by S_2 according its position towards S_1. The drag forces shown in the mapping present values with an accuracy of $\pm$ 1.1 mN. Some locations on the map lack of measures to be sufficiently well interpolated, this is why the mapping has to be taken with cautious.

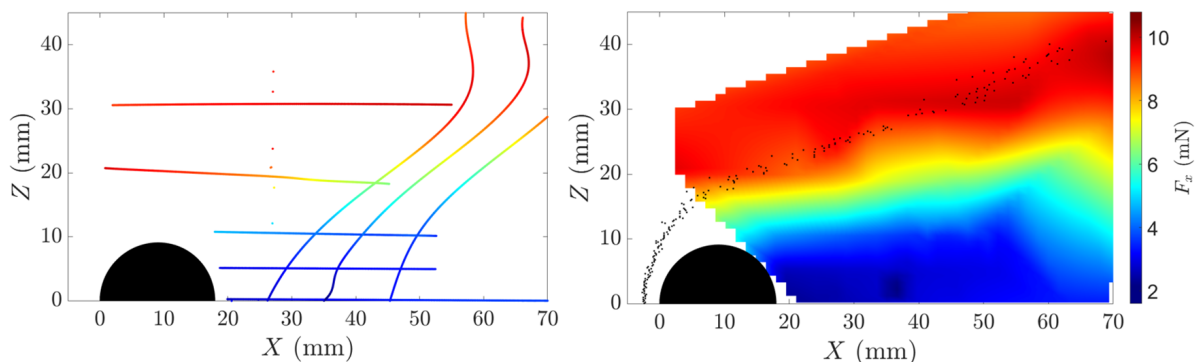**Fig 14.** Corrected drag forces of S_2 flying around S_1. Left: plot of the mean trajectory of S_2 associated to the values of drag force. Right: 2D mapping of the interpolated drag forces

The middle of shock of S_1 has been plotted on the map. As can be observed, the highest values of drag

force are located around the shock. There is almost no difference between the forces measured in the free-stream and those measured in the shock wave. This means that the impact of S_1 shock wave on the drag of the following sphere is slight. But analyzing the jet normalized images of Fig.6, it lets to think that the lift forces should be more impacted. Consequently the trajectory of S_2 towards S_1 would be influenced. A deeper investigation on forces is necessary to better understand the behavior of S_2 in such interacting conditions.

5. Conclusion and perspectives

Shock/shock interferences were investigated for two spheres flying in a Mach 20.2 rarefied flow with a free-stream pressure of 0.07 Pa. Such conditions, obtained in the MARHy wind tunnel, allowed to experimentally simulate two proximal bodies of about 1 m flying at 95 km in Earth's atmosphere.

Through flow-field visualization some differences were observed according the different relative positions between the two spheres. It seems that the shock/shock interferences are different from the ones presented by Edney, and previously observed by the authors in a less rarefied flow. Here it is preferable to talk about a shock/shock mixing layer since no shock deformation seems clear enough to identify different types of interferences. An investigation with electron gun will hopefully help better visualize flow-field and measure local density in the interference area. Based on the analysis of luminous intensity, results tends to demonstrate a real variation of the local density in the following sphere (S_2) boundary layer. This lets think that the maximal values of pressure at the wall of S_2 will be mainly located on upper part of its surface; except for the case where S_2 is mostly above the shock wave of S_1 ($\Theta_i >$ -20°). A wall pressure investigation is being realized to confirm this statement.

The pendulum technique allowed to obtain a mapping of the drag forces of S_2 in proximity with S_1. It showed that the impact of the incident shock-wave is low but still exists, increasing the drag forces of S_2 of about 10%. A further investigation will consist in measuring the lift forces to complete the precedent point and the wall pressure investigation. Such results will help predict the modification of trajectory induced by shock/shock interferences in these experimental conditions.

References

[1] B Edney, "Anomalous heat transfer and pressure distributions on blunt bodies at hypersonic speeds in the presence of an impinging shock," Tech. Rep., Flygtekniska Forsoksanstalten, Stockholm (Sweden), 1968.

[2] J Délery and J P Dussauge, "Some physical aspects of shock wave/boundary layer interactions," *Shock waves*, vol. 19, no. 6, pp. 453, 2009.

[3] M Holden, S Sweet, J Kolly, and G Smolinski, "A review of the aerothermal characteristics of laminar, transitional and turbulent shock/shock interaction regions in hypersonic flows," in *36th AIAA Aerospace Sciences Meeting and Exhibit*, 1998, p. 899.

[4] J J Bertin and R M Cummings, "Critical hypersonic aerothermodynamic phenomena," *Annual Review of Fluid Mechanics*, vol. 38, pp. 129–157, 2006.

[5] A B Carlson and R G Wilmoth, "Shock interference prediction using direct simulation monte carlo," *Journal of Spacecraft and Rockets*, vol. 29, no. 6, pp. 780–785, 1992.

[6] A Gülhan, S Willems, and D Neeb, "Shock interaction induced heat flux augmentation in hypersonic flows," *Experiments in Fluids*, vol. 62, no. 12, pp. 1–18, 2021.

[7] John Harvey, Michael Holden, and Timothy Wadhams, "Code validation study of laminar shock/boundary layer and shock/shock interactions in supersonic flow part b: Comparison\ith navier-stokes and dsmc solutions," in *39th Aerospace Sciences Meeting and Exhibit*, 2001, p. 1031.

[8] G Klopfer and H Yee, "Viscous hypersonic shock-on-shock interaction on blunt cowl lips," in *26th Aerospace Sciences Meeting*, 1988, p. 233.

[9] D Knight, N Kianvashrad, and M R Youssefi, "Simulation of hypersonic shock wave laminar bounday layer interactions," in *11th Ankara International Aerospace Conference*, 2021.

[10] A R Wieting and M S Holden, "Experimental shock-wave interference heating on a cylinder at mach 6 and 8," *AIAA Journal*, vol. 27, no. 11, pp. 1557–1565, 1989.

[11] C White and K Kontis, "The effect of increasing rarefaction on the edney type iv shock interaction problem," in *International Conference on RailNewcastel Talks*. 2018, pp. 299–311, Springer, Cham.

[12] H Xiao, Y Shang, and D Wu, "Dsmc simulation and experimental validation of shock interaction in hypersonic low density flow," *The Scientific World Journal*, vol. 2014, 2014.

[13] J N Moss and G A Bird, "Direct simulation monte carlo simulations of hypersonic flows with shock interactions," *AIAA Journal*, vol. 43, no. 12, pp. 2565–2573, 2005.

[14] T Pot, B Chanetz, M Lefebvre, and P Bouchardy, "Fundamental study of shock/shock interference in low density flow: flowfield measurements by dlcars," in *RGD : rarefied gas dynamics (Marseille, 26-31 July 1998)*, 1999, pp. 545–552.

[15] V V Riabov and A V Botin, "Shock interference in hypersonic rarefied-gas flows near a cylinder," in *17th Applied Aerodynamics Conference*, 1999, p. 3207.

[16] Y Prevereaud, J L Vérant, J M Moschetta, F Sourgen, and M Blanchard, "Debris aerodynamic interactions during uncontrolled atmospheric reentry," in *AIAA Atmospheric Flight Mechanics Conference*, 2012, p. 4582.

[17] John T Emmert, Douglas Patrick Drob, J Michael Picone, David E Siskind, M Jones Jr, MG Mlynczak, PF Bernath, X Chu, E Doornbos, Bernd Funke, et al., "Nrlmsis 2.0: A whole-atmosphere empirical model of temperature and neutral species densities," *Earth and Space Science*, vol. 8, no. 3, pp. e2020EA001321, 2021.

[18] L Kovacs, P-Y Passaggia N, Mazellier, and V Lago, "Detection method for shock-waves in viscous flows," *Experiments in Fluids*, vol. 63, no. 1, pp. 1–16, 2022.

[19] V Cardona and V Lago, "Aerodynamic forces of interacting spheres representative of space debris re-entry: Experiments in a supersonic rarefied wind-tunnel," *Acta Astronautica*, vol. 191, pp. 148–159, 2022.

[20] H Noubel and V Lago, "Experimental analysis of waverider lift-to-drag ratio measurements in rarefied and supersonic regime," 2021.

[21] J Aroesty, "Sphere drag in low density supersonic flow," No. he-150-192, California Univ Berkley Inst of Engineering Research, 1962.

[22] A B Bailey and J Hiatt, "Sphere drag coefficients for a broad range of mach and reynolds numbers," *Aiaa Journal*, vol. 10, no. 11, pp. 1436–1440, 1972.

[23] P P Wegener and H Ashkenas, "Wind tunnel measurements of sphere drag at supersonic speeds and low reynolds numbers," *Journal of Fluid Mechanics*, vol. 10, no. 4, pp. 550–560, 1961.

[24] T Fisher, M K Quinn, and K Smith, "Free-flight testing of hypersonic edney shock interactions," in *2018 Aerodynamic Measurement Technology and Ground Testing Conference*, 2018, p. 4283.

[25] V Cardona, R Joussot, and V Lago, "Shock/shock interferences in a supersonic rarefied flow: experimental investigation," *Experiments in Fluids*, vol. 62, no. 6, pp. 1–14, 2021.

[26] V Cardona and V Lago, "The effect of rarefaction level on shock/shock interferences applied to atmospheric re-entry: experimental study in a supersonic rarefied flow," in *2nd International Conference on Flight Vehicles, Aerothermodynamics and Re-entry Missions and Engineering*, 2022.